

This is the accepted manuscript made available via CHORUS. The article has been published as:

Simulation study of twisted crystal growth in organic thin films

Alta Fang and Mikko Haataja

Phys. Rev. E **92**, 042404 — Published 15 October 2015

DOI: [10.1103/PhysRevE.92.042404](https://doi.org/10.1103/PhysRevE.92.042404)

Simulation study of twisted crystal growth in organic thin films

Alta Fang

*Department of Mechanical and Aerospace Engineering,
Princeton University, Princeton, New Jersey 08544, USA**

Mikko Haataja

*Department of Mechanical and Aerospace Engineering,
Princeton Institute for the Science and Technology of Materials (PRISM),
the Andlinger Center for Energy and the Environment (ACEE),
and Program in Applied and Computational Mathematics (PACM),
Princeton University, Princeton, New Jersey 08544, USA†*

Abstract

Many polymer and organic small-molecule thin films crystallize with microstructures that twist or curve in a regular manner as crystal growth proceeds. Here we present a phase-field model that energetically favors twisting of the three-dimensional crystalline orientation about and along particular axes, allowing morphologies such as banded spherulites, curved dendrites, and “s”- or “c”-shaped needle crystals to be simulated. When twisting about the fast-growing crystalline axis is energetically favored and spherulitic growth conditions are imposed, crystallization occurs in the form of banded spherulites composed of radially oriented twisted crystalline fibers. Due to the lack of symmetry, twisting along the normal growth direction leads to heterochiral banded spherulites with opposite twist handedness in each half of the spherulite. When twisting is instead favored about the axis perpendicular to the plane of the substrate and along the normal growth direction under diffusion-limited single-crystalline growth conditions, crystallization occurs in the form of curved dendrites with uniformly rotating branches. We show that the rate at which the branches curve affects not only the morphology but also the overall kinetics of crystallization, as the total crystallized area at a given time is maximized for a finite turning rate.

PACS numbers: 81.15.Aa, 68.55.-a

* alta@princeton.edu

† mhaataja@princeton.edu

I. INTRODUCTION

Organic thin films can crystallize in a wide array of complex morphologies, ranging from polycrystalline spherulites to single-crystalline dendrites [1], and the microstructure of a thin film can significantly affect its properties [2]. In particular, polymers as well as some organic small molecules tend to crystallize in the form of anisotropic ribbon-shaped lamella composed of folded polymer chains or stacked molecules, as geometric frustration leads these materials to form a kinetically trapped metastable structure. One phenomenon that has attracted considerable attention in these systems is twisted crystal growth, where the local crystalline orientation gradually varies in space, turning consistently in one direction as growth proceeds [3, 4]. One common example of twisting occurs in some spherulites that exhibit concentric ring bands when viewed under an optical microscope. Many of these banded spherulites have been shown to be composed of radially oriented helically twisting lamella, as demonstrated by circular birefringence, AFM, and SEM images [5, 6]. Other curved crystallization morphologies, such as dendrites with uniformly rotating branches, have been observed in poly(L-lactide)/poly(D-lactide) (PLLA/PDLA) blend thin films [7, 8].

Multiple theories have been proposed for the mechanisms of twisted crystallization, including bending moments induced by mismatched lamellar surface stresses due to tilt of the polymer chain folding direction relative to the lamellar surface [9, 10], self-induced compositional or mechanical fields that lead crystal growth to occur faster if twisting occurs [11, 12], and autodeformation due to heterometry strains where inhomogeneities lead to strains that multiply through positive feedback [3, 13]. The reasons for twisting are thus still not fully understood, and it is likely that different causes for twisting are active under different conditions [3, 4].

Modeling efforts so far have focused on understanding how and why individual lamella twist [10, 11, 14, 15], but less work has been done on modeling their collective behavior [6, 16]. The larger-scale crystallization morphologies of these systems can be complex, since in twisted banded spherulites, lamella not only twist but also splay and may twist with different chirality in different regions of the spherulite. To model the formation of these crystallization patterns, one can simply assume that there exists a thermodynamic driving force for twisting without necessarily specifying the mechanism for twisting. Phase-field modeling represents a promising approach to study crystal growth under this assumption,

since it uses physically based phenomenological expressions to describe the thermodynamics and kinetics of a system. Indeed, phase-field models have already been used to extensively reproduce a variety of spherulitic and dendritic polycrystalline morphologies [17], simulate banded spherulites that result from rhythmic growth [18, 19], and model ripple formation during polymer crystallization [20], but they have not until now been extended to study twisting behavior.

Motivated by the many experimentally observed occurrences of twisting in thin film crystallization, here we present a model that postulates a thermodynamic free energy that favors a constant rate of orientational twisting in the crystalline phase. We use a phase-field model to study pattern formation on length scales of tens to hundreds of microns without resolving the details of individual molecules or lamella. Here we treat films as two-dimensional (2D) since we assume films to be uniform through their thicknesses, and we treat the initial state of a film as a disordered amorphous phase such as a melt, which subsequently undergoes a first-order phase transition to a crystalline phase.

We demonstrate that our model can simulate a wide array of twisting and curving crystal morphologies that resemble those seen in experiments, including banded spherulites, curved dendrites, and “c”-shaped or “s”-shaped crystals. Heterochiral banded spherulites, in which twisting occurs with opposite handedness in either half of the spherulite, form when twisting is energetically favored about the fast-growing crystalline axis and along the direction of crystal growth. Curved dendrites with branches that all turn in the same direction form when twisting is energetically favored about the axis perpendicular to the substrate and along the direction of crystal growth. The rate of orientational turning in curved dendrites is found to affect not only the morphology but also the kinetics of crystallization, with a maximum areal growth achieved for a given crystallization time with a specific, finite turning rate.

The rest of the manuscript is organized as follows. Section II describes our modeling framework, while simulation results are presented in Sec. III. Finally, Sec. IV gives a summary and concluding remarks.

II. MODEL

A. Phase-field modeling framework

Our model is based on a phase-field modeling technique that has previously been used to simulate solidification processes [21]. We begin by defining a crystallinity order parameter $\phi(\vec{r}, t)$, where $\phi = 1$ ($\phi = 0$) denotes the crystalline (amorphous) phase. We also introduce a unit quaternion field $\vec{q}(\vec{r}, t) = [q_0, q_1, q_2, q_3]$ that represents the local three-dimensional (3D) crystalline orientation, which is defined throughout the whole domain, including the amorphous phase [22–25]. We construct the following free energy functional:

$$F = \int d\vec{r} \left[\frac{\epsilon_\phi^2}{2} |\vec{\nabla} \phi|^2 + f(\phi, u) + p(\phi) \left(\frac{\epsilon_q^2}{2} \sum_{i=0}^3 \left| \vec{\nabla} q_i - t_i(\vec{q}, \hat{w}, P) \hat{s} \right|^2 + h(\vec{q}) \right) \right] \quad (1)$$

where

$$f(\phi, u) = \frac{\phi^4}{4} + \frac{m(u) - 3/2}{3} \phi^3 - \frac{m(u) - 1/2}{2} \phi^2, \quad (2)$$

$$m(u) = \frac{\alpha}{\pi} \tan^{-1}(-\gamma u), \quad (3)$$

$$p(\phi) = \phi^3(10 - 15\phi + 6\phi^2), \quad (4)$$

and

$$h(\vec{q}) = b(1 - \cos(4\varphi)) + \lambda(\cos^2 \varphi - 1/2), \quad (5)$$

where

$$\varphi = \cos^{-1}(g_{33}) \quad (6)$$

and \hat{s} is the axis along which twisting occurs, while \hat{w} is the axis about which twisting occurs.

The crystalline orientation represented by a unit quaternion \vec{q} is the orientation achieved by applying a rotation described by \vec{q} to the fixed substrate reference frame $\{\hat{x}_s, \hat{y}_s, \hat{z}_s\}$. Specifically, in Cartesian coordinates, the rotation transformation to arrive at the crystalline axes $\{\hat{x}_c, \hat{y}_c, \hat{z}_c\}$ from the substrate axes is given by:

$$R = \begin{bmatrix} g_{11} & g_{21} & g_{31} \\ g_{12} & g_{22} & g_{32} \\ g_{13} & g_{23} & g_{33} \end{bmatrix} = \begin{bmatrix} q_0^2 + q_1^2 - q_2^2 - q_3^2 & 2(q_1 q_2 - q_0 q_3) & 2(q_1 q_3 + q_0 q_2) \\ 2(q_1 q_2 + q_0 q_3) & q_0^2 - q_1^2 + q_2^2 - q_3^2 & 2(q_2 q_3 - q_0 q_1) \\ 2(q_1 q_3 - q_0 q_2) & 2(q_2 q_3 + q_0 q_1) & q_0^2 - q_1^2 - q_2^2 + q_3^2 \end{bmatrix}. \quad (7)$$

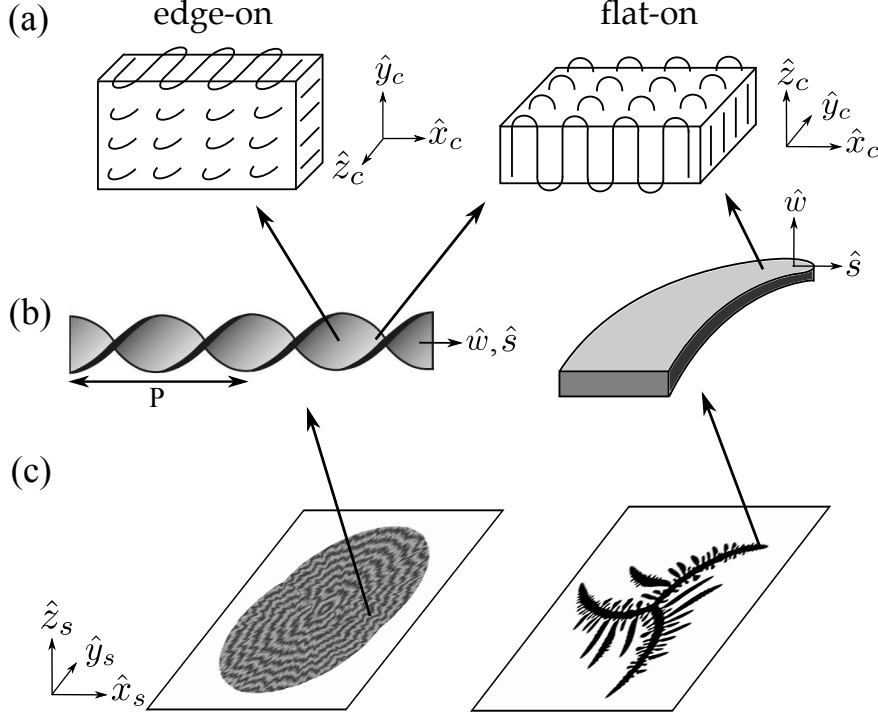


FIG. 1. Schematic of crystallization geometry. (a) A set of axes $\{\hat{x}_c, \hat{y}_c, \hat{z}_c\}$ is attached to a crystalline lamella to track its local 3D orientation. When \hat{z}_c is parallel (perpendicular) to the plane of the substrate, the orientation is edge-on (flat-on). (b) A twisted lamella in a banded spherulite alternates between edge-on and flat-on orientations, rotating 360° over a period P about the axis \hat{w} and along the axis \hat{s} , which in this case are parallel. The helix schematic is adapted from Ref. 26. The orientation of a curved flat-on dendrite branch also rotates about \hat{w} and along \hat{s} , which in this case are orthogonal. (c) Attached to the thin films are fixed substrate axes $\{\hat{x}_s, \hat{y}_s, \hat{z}_s\}$.

Crystalline axes $\{\hat{x}_c, \hat{y}_c, \hat{z}_c\}$ are attached to a polymer lamella such that \hat{z}_c is perpendicular to the disordered fold surface of the lamella, while \hat{x}_c and \hat{y}_c lie in the chain folding plane with \hat{x}_c aligned with the fast-crystallizing direction, as shown in Fig. 1(a). [Note that although the schematic shows a chain-folded polymer, this alignment can be applied to any material that crystallizes in a similar structure.] Here we identify the lamellar orientation with the crystalline orientation and do not explicitly account for chain tilt, which occurs when chain-folding stems are not perfectly aligned with lamellar surface normals [10].

The free energy functional F includes terms accounting for the presence of crystal-amorphous interfaces, the bulk free energy of crystallization, and the orientational energy

in the crystalline phase. Crystal-amorphous interface energy is incorporated via the term $\epsilon_\phi^2 |\vec{\nabla}\phi|^2/2$, while the bulk free energy of crystallization is given by $f(\phi, u)$ and has the form of a double-well potential in the crystallinity order parameter ϕ , following Ref. 21. In the present work, $u(\vec{r}, t)$ is a field analogous to the non-dimensionalized temperature which incorporates diffusion-limited transport processes and which will be further explained below, while α and γ are parameters that control how u and ϕ are coupled. A monotonically increasing interpolating polynomial $p(\phi)$ modulates the orientational terms to only affect the free energy in the crystalline phase because $f(\phi, u)$ already captures the energetic costs of misorientations in the amorphous phase [22].

The misorientation energy in the crystalline phase is accounted for through a squared gradient term in $\vec{\nabla}q$ that energetically favors a twist rate $\vec{t}(\vec{q}, \hat{w}, P)$ along the direction \hat{s} and about the axis \hat{w} with period P ; the numerical formula for calculating $\vec{t}(\vec{q}, \hat{w}, P)$ will be described below. Note that here we use a term that is squared rather than linear in $\vec{\nabla}q$ because twisting is often experimentally observed to occur in a continuous manner [3]. This form of the misorientation energy effectively treats the stable phase as liquid crystalline rather than crystalline, since it permits no finite-width stable grain boundaries [27]. However, because we use kinetics to freeze in misorientations at the growth front, we find that this form of the free energy can still lead to effectively polycrystalline microstructures composed of regions of different crystalline orientations. Also note that \hat{s} and \hat{w} may depend on the crystallinity order parameter ϕ , providing another coupling between the orientational and crystallinity order parameters. In fact, in many of the numerical simulations to be discussed below, $\hat{s} = \frac{-\vec{\nabla}\phi}{|\vec{\nabla}\phi|}$.

Since polymer thin films tend to crystallize with lamella arranged in either a flat-on or edge-on out-of-plane orientation [1], we introduce a term $h(\vec{q})$ that energetically favors either the edge-on or flat-on orientations, which correspond respectively to the \hat{z}_c axis aligned either parallel or perpendicular to the plane of the substrate, as shown in Fig. 1(a). The parameter b dictates the height of the energetic barrier between the favored out-of-plane orientations while λ controls which orientation is more energetically favorable. We envision that λ depends on for example the processing conditions [28] or film thickness [1], and have previously used a similar approach to simulate a variety of non-twisting/curving polycrystalline microstructures in thin films [29, 30].

Given the free energy functional above, the time evolution is computed as follows:

$$\begin{aligned} \frac{\partial \phi}{\partial t} = M_\phi \left[\epsilon_\phi^2 \nabla^2 \phi - \frac{\partial f}{\partial \phi} - p'(\phi) \left(\frac{\epsilon_q^2}{2} \sum_{i=0}^3 \left| \vec{\nabla} q_i - t_i(\vec{q}, \hat{w}, P) \hat{s} \right|^2 + h(\vec{q}) \right) + \right. \\ \left. \frac{\epsilon_q^2}{2} \vec{\nabla} \cdot \left(p(\phi) \frac{\partial}{\partial \vec{\nabla} \phi} \sum_{i=0}^3 \left| \vec{\nabla} q_i - t_i(\vec{q}, \hat{w}, P) \hat{s} \right|^2 \right) \right], \end{aligned} \quad (8)$$

$$\frac{\partial q_i}{\partial t} = -M_q \left[\frac{\delta F}{\delta q_i} - \frac{q_i}{\sum_{j=0}^3 q_j^2} \sum_{k=0}^3 q_k \frac{\delta F}{\delta q_k} \right] \quad (9)$$

with

$$\begin{aligned} \frac{\delta F}{\delta q_i} = -\epsilon_q^2 \vec{\nabla} \cdot \left[p(\phi) \left(\vec{\nabla} q_i - t_i(\vec{q}, \hat{w}, P) \hat{s} \right) \right] + \\ p(\phi) \left(\frac{\partial h}{\partial q_i} + \frac{\epsilon_q^2}{2} \frac{\partial}{\partial q_i} \sum_{j=0}^3 \left| \vec{\nabla} q_j - t_j(\vec{q}, \hat{w}, P) \hat{s} \right|^2 \right), \end{aligned} \quad (10)$$

and

$$\frac{\partial u}{\partial t} = D \nabla^2 u + \frac{1}{\Delta} \frac{\partial \phi}{\partial t}, \quad (11)$$

where Lagrange multipliers have been used to enforce the unit length of the quaternions [22–25]. Note that time-dependent fluctuations are not included in Eqs. (8) and (9), since initializing the amorphous phase with random orientations at each point provides sufficient noise at the crystal-amorphous interface to simulate the growth of spherulites and dendrites.

The field $u(\vec{r}, t)$ in Eq. (11) is analogous to the dimensionless temperature in solid-liquid phase transformations [21, 29, 31]. It allows us to simulate diffusion-limited conditions that lead to dendritic or seaweed-like structures. We envision that physically the conserved quantity in single-component films is the molecule itself, as densification may lead to a depletion of crystallizable material ahead of the crystal growth front. Furthermore, Δ is a tunable parameter controlling the degree of diffusion limitation, with a lower value of Δ corresponding to a greater degree of diffusion limitation. More specifically, given the boundary conditions employed in the simulations and upon setting $u = -1$ initially, for $0 < \Delta < 1$, a fraction Δ of the system will crystallize before the effective undercooling is exhausted, while setting $\Delta \gg 1$ gives rise to compact crystallites that span the whole system [32]. The u field is in turn coupled with the free energy through $m(u)$ so that as u increases

from -1 to 0, the driving force for crystallization decreases from its initial value to zero due to depletion of the conserved quantity.

The crystallization mobility M_ϕ in Eq. (8) is modulated to account for a k -fold-symmetric crystalline anisotropy of magnitude δ . This reflects that organic materials often have anisotropic structures such that crystal growth proceeds faster along particular directions [7, 33]. Furthermore, we eliminate all post-crystallization grain growth or coarsening processes by modulating the orientational mobility M_q in Eq. (9) to be zero in the crystalline phase, consistent with experimental observations [33, 34]. Thus the mobilities of the crystalline and quaternion fields are given by

$$M_\phi = M_{\phi,0} [1 + \delta \cos(k\theta)] \quad (12)$$

$$M_q = M_{q,0} [1 - p(\phi)] \quad (13)$$

where

$$\theta = \cos^{-1}(\hat{n} \cdot \hat{x}_c) \quad (14)$$

$$\text{and } \hat{n} = \frac{-\vec{\nabla}\phi}{|\vec{\nabla}\phi|} \quad (15)$$

subject to the constraint that $0 \leq \delta < 1$. Note that although we introduce anisotropy into the crystallization mobility, we do not account for crystalline symmetries in our calculations of quaternion misorientations as has been previously suggested [22], since we have found that doing so leads to pinned topological defects in the orientation field and is also not necessary to produce symmetric crystal shapes. Indeed, some of the twisting morphologies simulated below, such as heterochiral banded spherulites, require a lack of crystalline symmetry. In general, a crystal may have multiple fast-growing directions that are nevertheless not crystallographically equivalent. Also note that we do not incorporate any anisotropy in the surface energy, as the anisotropy in M_ϕ is sufficient to generate dendritic morphologies under diffusion-limited conditions.

B. Numerical implementation

We numerically implement our model using explicit finite difference time-stepping on a uniform 2D grid with periodic boundary conditions for ϕ and \vec{q} and no-flux boundary conditions for u . Laplacians are calculated with a 9-point stencil and spatial derivatives of

the quaternion field are calculated using the finite volume formulas described in Appendix A, which use information from corner grid points to provide a more isotropic implementation of the derivatives. We initialize the film in the amorphous phase with random orientations on each grid point following the algorithm in Ref. 35 and then place a small crystalline seed with prescribed orientation \vec{q}_{init} in the center of the simulation box. Since \vec{q} and $-\vec{q}$ correspond to equivalent orientations, when calculating spatial derivatives of \vec{q} we use the sign of $\vec{q}_{neighbor}$ such that $\vec{q}_{neighbor} \cdot \vec{q}_{center} > 0$, where $\vec{q}_{neighbor}$ is the quaternion value in the neighboring grid point and \vec{q}_{center} is the quaternion in the grid point currently being calculated. At each time step the quaternions are renormalized to ensure that they remain unit length throughout the simulation, since using Lagrange multipliers alone results in numerical errors accumulating to produce a drift in quaternion length.

The components of the energetically favored quaternion twist rate $\vec{t}(\vec{q}, \hat{w}, P)$ are calculated by:

$$t_i(\vec{q}, \hat{w}, P) = \frac{q'_i(\vec{q}, \hat{w}, \theta_t) - q_i}{\Delta x}, \quad (16)$$

where

$$\vec{q}'(\vec{q}, \hat{w}, \theta_t) = \left[q_0 \cos \frac{\theta_t}{2} - q_1 w_x \sin \frac{\theta_t}{2} - q_2 w_y \sin \frac{\theta_t}{2} - q_3 w_z \sin \frac{\theta_t}{2}, \quad (17)$$

$$q_1 \cos \frac{\theta_t}{2} + q_0 w_x \sin \frac{\theta_t}{2} + q_3 w_y \sin \frac{\theta_t}{2} - q_2 w_z \sin \frac{\theta_t}{2}, \quad (18)$$

$$q_2 \cos \frac{\theta_t}{2} - q_3 w_x \sin \frac{\theta_t}{2} + q_0 w_y \sin \frac{\theta_t}{2} + q_1 w_z \sin \frac{\theta_t}{2}, \quad (19)$$

$$q_3 \cos \frac{\theta_t}{2} + q_2 w_x \sin \frac{\theta_t}{2} - q_1 w_y \sin \frac{\theta_t}{2} + q_0 w_z \sin \frac{\theta_t}{2} \right]. \quad (20)$$

In the limit $\theta_t \rightarrow 0$ and $\Delta x \rightarrow 0$, this quaternion twist rate corresponds to a continuous rotation by 2π over a period of length $P = \frac{2\pi}{\theta_t} \Delta x$, as shown in Fig. 1(b) for a twisting lamella. This formula for \vec{t} arises from rotating in a distance Δx the local quaternion $\vec{q} = [q_0, q_1, q_2, q_3]$ by an angle θ_t about the axis $\hat{w} = (w_x, w_y, w_z)$ to obtain the rotated quaternion \vec{q}' , which is calculated by composing the twist rotation $\vec{p} = \left[\cos \frac{\theta_t}{2}, w_x \sin \frac{\theta_t}{2}, w_y \sin \frac{\theta_t}{2}, w_z \sin \frac{\theta_t}{2} \right]$ with the original rotation \vec{q} using quaternion Hamilton multiplication [36]: $\vec{q}' = \vec{p}\vec{q}$.

For many of the simulations presented below, we energetically favor twisting along the normal growth direction, i.e. $\hat{s} = \hat{n} = \frac{-\vec{\nabla}\phi}{|\vec{\nabla}\phi|}$. This causes the growth direction \hat{n} to appear in the free energy functional even though it is undefined in the bulk phases. In our numerical implementation, when the value of $|\vec{\nabla}\phi|$ is below a threshold value of d_{cutoff} , we set $1/|\vec{\nabla}\phi|$

equal to a constant value of $1/d_{cutoff}$. Furthermore, the last term in Eq. (8) is set to zero for $\phi > \phi_{cutoff}$, since we imagine that in the crystalline phase, the direction along which twisting is energetically favored, \hat{s} , is a constant equal to the value of \hat{n} at the time the growth front passed, which the crystal can “remember” through plastic deformation. Thus, since \hat{s} no longer depends on $\vec{\nabla}\phi$ in the crystalline phase, the last term in Eq. (8) can be set to zero for $\phi > \phi_{cutoff}$.

In our simulations we use the following non-dimensionalized parameter values: $N_x = N_y = 1024$, $\Delta x = \Delta y = 0.01$, $\Delta t = 8 \times 10^{-7}$, $\alpha = 0.9$, $\gamma = 10$, $D = 1$, $M_{\phi,0} = 1.5 \times 10^4$, $\epsilon_\phi^2 = 2 \times 10^{-5}$, $\epsilon_q^2 = 1 \times 10^{-5}$, $d_{cutoff} = 1 \times 10^{-3}$, $\phi_{cutoff} = 0.95$. These parameter values were chosen to produce physically reasonable outputs, since we aim to study the general behavior of this model rather than simulate a particular material. The value of ϵ_q was chosen to be close to ϵ_ϕ , following other orientational phase-field models [24, 25, 37], and increasing ϵ_q has an effect similar to increasing M_q . Results are not sensitive to the value of d_{cutoff} , which can be any small number, since ϕ and \vec{q} evolve only at the interface.

III. RESULTS

A. Heterochiral banded spherulites

First, we simulate the growth of banded spherulites composed of radially aligned lamella that twist between edge-on and flat-on orientations, as illustrated in Fig. 1. Note that in general, banding in spherulites may result from either rhythmic growth, twisting, or a combination of the two [38, 39], but here we only consider twisting. Heterochiral banded spherulites, which have two halves that twist with opposite chirality, have been observed experimentally in, e.g., aspirin [6, 40] and poly(trimethylene terephthalate) (PTT) [41] thin films. In our model, heterochiral banded spherulites are simulated by energetically favoring twisting about the fast-growing crystalline axis, i.e., $\hat{w} = \hat{x}_c$, and along the normal growth direction, i.e., $\hat{s} = \hat{n}$. We introduce a moderately large 2-fold-symmetric mobility anisotropy $\delta = 0.75$ to reflect that crystallization occurs fastest in directions either parallel or antiparallel to the crystalline \hat{x}_c axis. Here we use $\Delta = 20$ to simulate compact spherulites, which have tightly packed lamella and grow in a kinetically-limited rather than diffusion-limited manner. A relative orientational mobility of $M_{q,0}/M_{\phi,0} = 17.5$ is used to allow random ori-

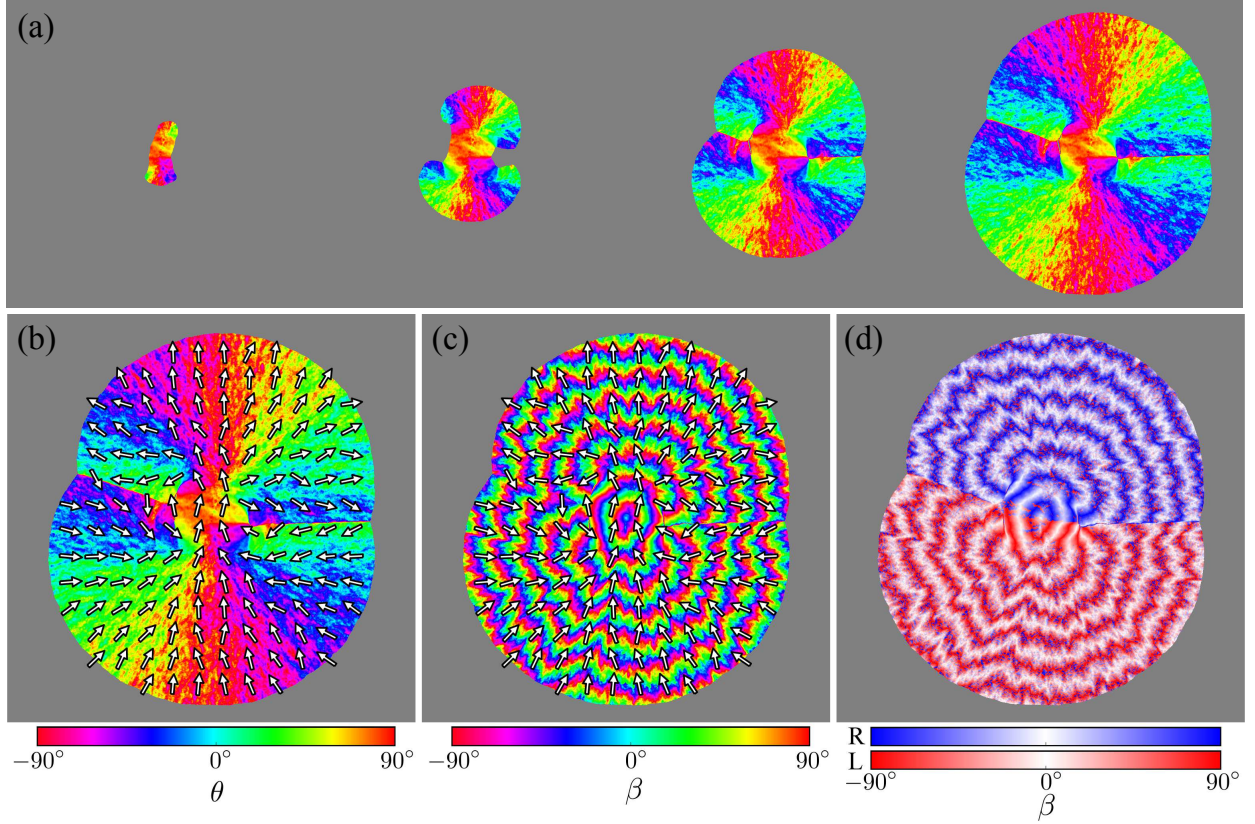


FIG. 2. (Color online) (a) Snapshots of the growth of a heterochiral banded spherulite at 40000, 80000, 120000, and 160000 time steps. The colors in the crystalline phase represent the in-plane lamellar orientation angle θ of the fast-growing crystalline direction \hat{x}_c , while the amorphous phase is shown in gray. (b) A plot of θ with overlaid arrows showing the in-plane direction of \hat{x}_c , which is aligned with the radial growth direction. (c) The out-of-plane lamellar orientation angle β twists between edge-on ($\beta = 0^\circ$) and flat-on ($\beta = \pm 90^\circ$) orientations. Overlaid is the same arrow field as in (b). (d) The top (bottom) half of the spherulite exhibits twisting with right-handed (left-handed) chirality. Note the formation of a “seam” where the chirality changes abruptly.

entations in the amorphous phase to be frozen into the growth front, since radial splaying in spherulitic growth occurs by non-crystallographic branching due to growth front nucleation [42]. Here we do not favor particular out-of-plane orientations and thus set $\lambda = 0$ and $b = 0$.

As shown in Fig. 2, simulated heterochiral banded spherulites exhibit both alignment of the fast-growing crystalline \hat{x}_c direction with the radial growth direction and periodic banding due to twisting, which occurs with opposite chirality on either side of the spherulite. Figures 2(a) and (b) use color to plot the angle of \hat{x}_c in the plane of the substrate, $\theta =$

$\tan^{-1}\left(\frac{g_{12}}{g_{11}}\right)$, yielding images similar to experimentally obtained polarized optical micrographs [5]. Amorphous regions are shown in gray. As shown in Fig. 2(a), the spherulite grows by splaying outwards from an initially needle-shaped seed, forming two halves with a boundary approximately perpendicular to the \hat{x}_c orientation of the initial seed, which in this simulation was oriented vertically. Figure 2(b) plots θ for the final configuration with overlaid arrows indicating the in-plane direction of \hat{x}_c , while Fig. 2(c) shows a color plot of the out-of-plane orientation angle $\beta = \tan^{-1}\left(\frac{\text{sign}(g_{33})\sqrt{g_{21}^2 + g_{22}^2}}{g_{23}}\right)$ between the crystalline axis \hat{y}_c and the substrate-perpendicular axis $\hat{z}_s \equiv (0, 0, 1)$, overlaid again with the same arrows showing \hat{x}_c . Note that there is no symmetry so \hat{x}_c and $-\hat{x}_c$ are not equivalent. Thus, in the upper half of the spherulite β decreases along the direction of \hat{x}_c , giving right-handed twisting, while in the lower half of the spherulite β increases along \hat{x}_c , giving left-handed twisting, with an accompanying “seam” where the chirality changes abruptly. This difference in chirality is highlighted in Fig. 2(d), which again shows β , now with saturated colors representing flat-on orientations and white representing edge-on orientations. Right-handed twisting is plotted in blue and left-handed twisting is plotted in red, producing a plot similar to experimentally obtained circular birefringence micrographs [5, 6, 40]. Here the chirality is determined by the sign of the dot product of \hat{x}_c with the gradient of β : $\text{chirality} = \text{sign}\left(g_{11}\frac{\partial\beta}{\partial x} + g_{12}\frac{\partial\beta}{\partial y}\right)$.

Figures 3(a) and (b) show that, as expected, the average observed twist periodicity in the banded spherulites is determined by the energetically favored twist period P , which here is reported relative to the crystal-amorphous interface width ξ . The measured banding period is slightly larger than the energetically favored P because the free energy favors twisting along the normal growth direction and no twisting along the tangential direction, but the spherulites are not always perfectly circular so the axis along which twisting is favored is not always radially aligned, thus causing less twisting to occur than what is specified by P . We also observe that band jaggedness increases slightly as the relative orientational mobility M_q/M_ϕ decreases, since random orientations are more easily frozen into the crystalline phase when the relative orientational mobility is low. This represents only one mechanism for banding irregularity, however, since additional interactions between and inhomogeneities within lamella may also affect the organization of the bands in a banded spherulite [3], and increased viscosity has been observed to correlate both with increased and decreased

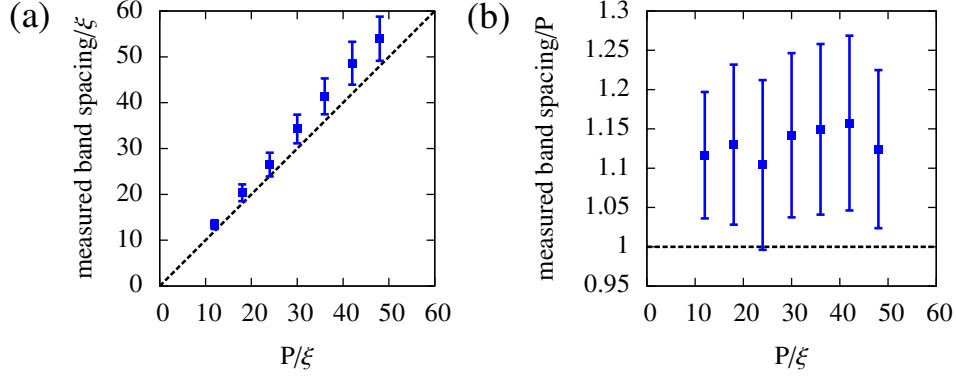


FIG. 3. (Color online) (a) The average measured band spacing in simulated heterochiral banded spherulites is shown as a function of the energetically favored twist period. The dashed line shows what the band spacing would be if it were exactly equal to the energetically favored value. Lengths are reported relative to the crystal-amorphous interface width ξ and error bars represent the standard deviation over measurements in 50° arcs on both sides of the spherulite. (b) The same data is plotted with the y-axis showing the ratio of the measured to the energetically favored period.

banding coherence under different circumstances [16].

B. Curved dendrites

Next, we simulate dendrites with uniformly rotating branches, which have been observed in, e.g., ultra-thin films of PLLA/PDLA blends [7, 8]. In our model, these curved dendrites arise when twisting of the crystalline orientation is energetically favored about an axis perpendicular to the substrate, i.e., $\hat{w} = \hat{z}_s$, and along the normal growth direction ($\hat{s} = \hat{n}$). Since ultra-thin films typically crystallize in a flat-on orientation, we energetically favor the flat-on orientation by setting $\lambda = -0.01$ and $b = 0.002$. A high relative orientational mobility $M_{q,0}/M_{\phi,0} = 200$ is used to reflect that, ignoring the curving, the dendrites are single-crystalline, as the time scale for orientational ordering is fast relative to the crystallization rate. Since crystallization is often diffusion-limited for these low film thicknesses and/or nonequimolar polymer blend ratios, here we set $\Delta = 0.5$. In the simulations below we use a mobility anisotropy of magnitude $\delta = 0.25$. Note that because these curved dendrites remain in a flat-on orientation, theoretically it is only necessary to track their local

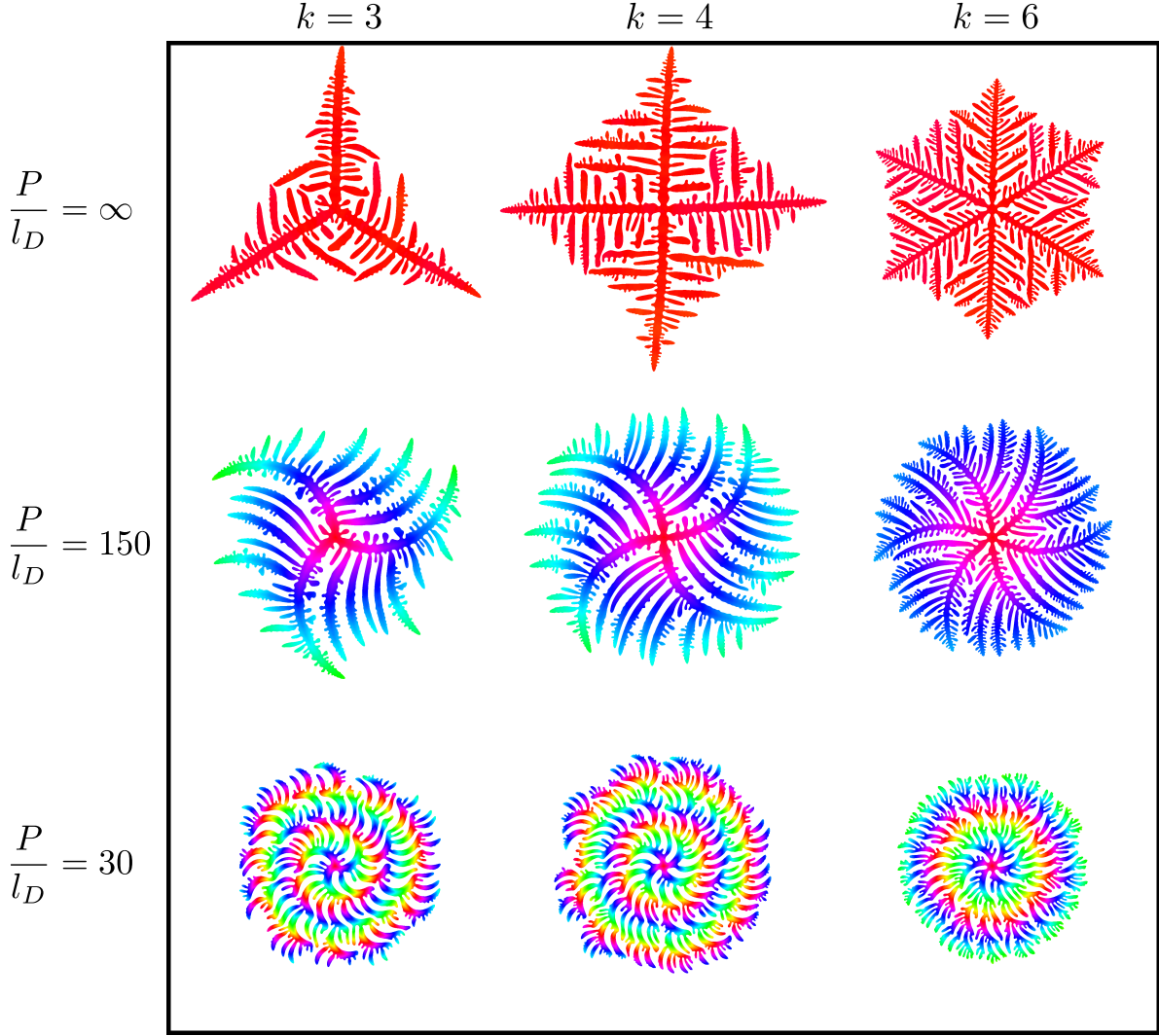


FIG. 4. (Color online) Dendrites with k -fold-symmetric mobility anisotropy curve as they grow with a radius of curvature dictated by the energetically favored orientational turning period P , which is here reported relative to the diffusion length $l_D = 2D/v$ of the straight dendrite for the respective value of k . Curving promotes the growth of side branches, which take over the propagation of the overall growth envelope after their parent branches have turned enough to collide with other branches. Colors represent the local in-plane orientation relative to a fixed substrate axis.

2D crystalline orientation, but here we continue to use the full 3D orientation in order to use the same modeling framework and to make it easier to extend these simulations to more general cases, such as when curved edge-on and flat-on crystals form simultaneously in the same film [7].

Figure 4 shows the morphologies that arise for different k -fold-symmetric kinetic anisotropies

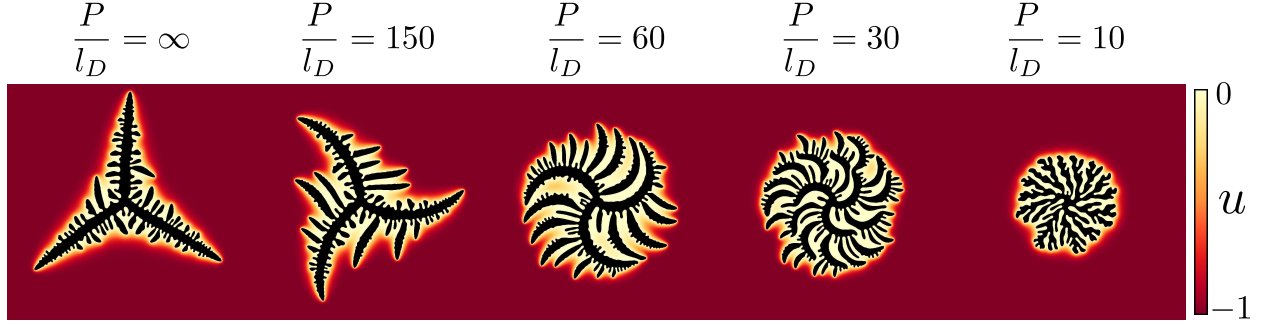


FIG. 5. (Color online) Simultaneous snapshots of dendrite growth for $k = 3$ for various energetically favored orientational turning rates with normalized periods P/l_D . When the radius of curvature $P/4$ becomes comparable to the branch width, the morphology becomes “seaweed”-shaped as the growth direction of the branches can no longer always locally match the crystalline orientation. The crystalline phase is shown in black, while in the amorphous phase the diffusing u field is shown with red (dark) indicating higher driving force for crystallization and yellow (light) indicating lower driving force for crystallization.

and different orientational turning rates, which are characterized by the period P over which the orientation turns by 360° . Lengths are reported relative to $l_D = \frac{2D}{v}$, the diffusion length of the non-curved dendrite for each value of k , where D is the diffusivity of the u field (equal to 1 in non-dimensionalized units), and v is the measured dendrite tip growth velocity for $P = \infty$ and fixed k . Colors represent $\theta = \tan^{-1} \left(\frac{g_{12}}{g_{11}} \right)$, the local in-plane orientation relative to a fixed substrate axis, and amorphous regions are shown in white. Due to the anisotropy, the turning of the crystalline orientation causes the branches to turn with a radius of curvature of approximately $P/4$, which is the distance over which θ varies by 90° . Side branching occurs preferentially on the side of parent branches facing away from the direction in which the branches turn, in agreement with experimental observations [7, 43]. Because the energetically preferred rotation period is constant, after turning by at most 180° , primary branches stop growing due to collision with other branches, and side branches take over the radially outward propagation of the growth envelope. These side branches grow until they too have turned so that their growth direction is perpendicular to the radial growth direction and the next generation of side branches then takes over.

Figure 5 in turn shows for the case of 3-fold-symmetric mobility anisotropy the morphologies that form within a fixed crystallization time for different orientational turning

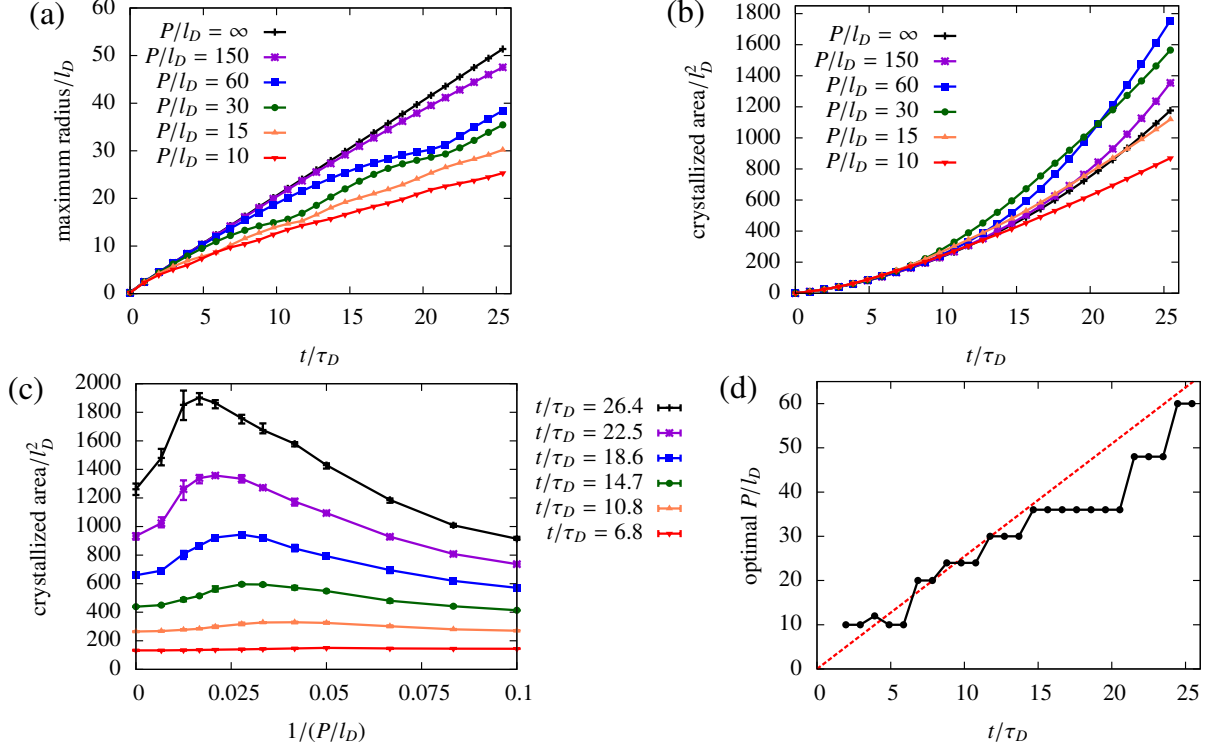


FIG. 6. (Color online) (a) The maximum radius of a dendrite, defined as the distance of the farthest crystallized point from the center, grows more slowly for greater twisting rates. (b) The total crystallized area increases with time at a rate that depends on the orientational turning period. (c) At each time, the crystallized area achieves a maximum at a particular turning period. As time progresses, this maximum occurs at larger periods. Plotted points and error bars correspond to the average, maximum, and minimum respectively over 3 initial conditions. (d) The orientational turning period at which the total crystallized area is maximized scales approximately as $P = \frac{4vt}{\pi}$ (red dashed line), which represents the turning period for which a branch would have turned by 180° at time t .

rates with normalized periods P/l_D , where l_D again denotes the measured diffusion length associated with the non-curved dendrite. The u field is plotted in the amorphous phase with larger gradients near the interface associated with larger local crystal growth rates, while the crystalline phase is shown in black. As the orientational turning period decreases, the branch radius of curvature also decreases until $P/4$ becomes comparable to the width of the branches, at which point the branch growth direction is no longer able to always locally align with the rapidly turning orientations in the crystalline phase, and the crystal takes

on a “seaweed”-like shape that resembles the morphology of diffusion-limited growth in the absence of any anisotropy [44]. The u field shows the diffusion-limited nature of the growth, as a region of reduced driving force, where u is closer to zero, builds up just ahead of the crystal growth front. As will be discussed next, observed changes in the growth morphology directly affect the large-scale crystallization kinetics.

It is well-known that needle crystals do not fill space effectively, while the more compact seaweed-like structures crystallize at a smaller rate relative to the needle crystals. In our simulations, the finite turning rate serves as an external knob which effectively controls the crystallization time after which simple anisotropic needle crystal growth becomes more isotropic, and one intuitively expects that this change in the large scale morphology of the crystal should be reflected in the overall growth kinetics. Indeed, not only do the morphologies vary with the orientational turning period, but the rates at which the position of the outermost crystallized point and the total crystallized area grow over time also depend on the turning rate, as shown in Fig. 6(a) and (b). Here, times are reported relative to the characteristic diffusion time $\tau_D = \frac{l_D^2}{D} = \frac{2l_D}{v}$ extracted from the simulations of the non-curved dendrite. Data for a 3-fold-symmetric mobility anisotropy is shown, but similar behavior was also observed for $k = 4$ and $k = 6$. The position of the outermost crystallized point grows linearly with time for the straight dendrite and in a slower oscillatory manner for intermediate turning periods, since branches approximately trace out circular arcs whose chord lengths vary as $\frac{P}{2} \sin\left(\frac{2v}{P}t\right)$ for $t < \frac{\pi P}{4v}$, after which a new generation of side branches takes over. For orientational turning periods small enough that the radius of curvature is comparable to the branch width, the morphology becomes seaweed-shaped, so that there are no longer distinct generations of turning branches and thus no longer any discernible oscillations in the tip position. Figure 6(b) shows that the total crystallized area also increases with time, but at a rate that varies non-monotonically with P/l_D . Figure 6(c) plots the same data as Fig. 6(b) but as a function of inverse orientational turning period for particular times, showing that at each time the total crystallized area is maximized at a finite turning period. As time progresses, the period at which this maximum occurs shifts so that at longer crystallization times lower rates of turning lead to the greatest crystallized area.

This variation in areal crystallization rate arises because the turning of the dendrite branches initially acts as an efficient method for guiding branches towards uncrystallized

regions with higher driving force for crystallization, leading to a faster areal growth rate than straight branch growth for a fixed tip growth rate. However, after the primary branches complete a turn of approximately 180° , the overall growth envelope becomes effectively isotropic so that diffusion limitations build up a region of low driving force for crystallization ahead of the growth front, slowing further growth. In the limit of a very high turning rate that results in a “seaweed” shape, branch tips become sufficiently rounded so that diffusion limitations slow growth even further. The orientational turning period for which the crystallized area is maximized at each time is shown in Fig. 6(d). Its scaling behavior can be approximated by $P = \frac{4vt}{\pi}$, which represents the turning period corresponding to branches that have turned by 180° at time t , assuming a constant local tip velocity v equal to that of the straight dendrite primary branch tip.

These results suggest that if the nucleation rate is also taken into consideration, the orientational turning rate can be optimized to achieve the most rapid areal crystallization rate for fixed values of all other parameters. Experimentally, the radius of curvature of dendrite branches in PLLA/PDLA blend thin films has been tuned by varying the blend ratio, film thickness, or crystallization temperature, although varying these parameters also simultaneously affected other crystallization properties [7]. It has also been suggested theoretically that curved dendrites can be engineered in thin films through the placement of uniformly rotating orientational pinning centers [45]. Our results demonstrate that varying the orientational turning rate of crystals growing in a diffusion-limited condition affects not only the crystallization morphology but also the kinetics.

C. Other morphologies

Finally, Fig. 7 summarizes four types of twisting or curving morphologies our model can simulate. Banded spherulites, plotted using the same color scheme as Fig. 2(d), may be either heterochiral, as shown in Fig. 7(a), or homochiral, as shown in Fig. 7(b). Heterochiral banded spherulites were discussed above in Sec. III A. Homochiral banded spherulites, in which all lamella twist with the same handedness, have been observed experimentally in microbial poly(R-3-hydroxybutyrate) copolymer films [14] and mannitol crystallized in the presence of poly(vinylpyrrolidone) or sorbitol [46]. In our model, homochiral banded spherulites can be simulated by favoring twisting about the fast-growing crystalline axis, i.e., $\hat{w} = \hat{x}_c$, and

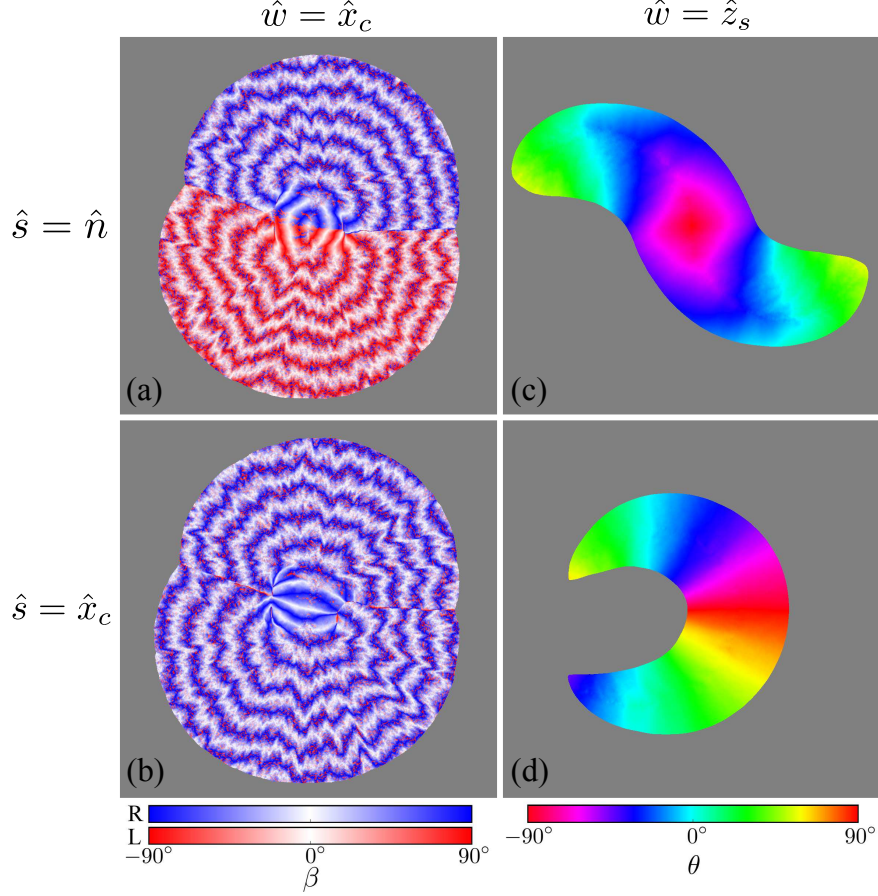


FIG. 7. (Color online) Four different types of twisting or curving morphologies are simulated for different axes about which (\hat{w}) and along which (\hat{s}) twisting is energetically favored: (a) heterochiral banded spherulites, (b) homochiral banded spherulites, (c) “s”-shaped crystals, and (d) “c”-shaped crystals.

along the same axis, i.e., $\hat{s} = \hat{x}_c$.

Another class of curved crystallization morphologies arises when orientational twisting occurs instead about the axis perpendicular to the plane of the substrate with a 2-fold-symmetric anisotropy of magnitude $\delta = 0.75$ and under single-crystal-forming conditions where $M_{q,0}/M_{\phi,0} = 200$: “s”-shaped or “c”-shaped crystals, as shown in Fig. 7(c) and Fig. 7(d) respectively. The “s”-shaped crystal is analogous to the curved dendrites discussed above, but with $k = 2$, $\Delta = 20$, and $\delta = 0.75$. The “c”-shaped crystal in Fig. 7(d) forms when twist occurs about the axis perpendicular to the substrate, i.e., $\hat{w} = \hat{z}_s$, and the direction along which twist occurs is given by the fast-growing crystalline direction, i.e., $\hat{s} = \hat{x}_c$. Experimentally, “s”-shaped crystals have been observed in ultra-thin films of poly(ϵ -

caprolactone)/poly(vinyl chloride) blends [47], while morphologies similar to the “c”-shaped crystal, albeit with spatially varying curvature and multiple branches, have been observed in ultra-thin films of linear low-density polyethylene [48].

An even wider array of morphologies can in theory be engineered by applying time-varying or spatially-varying treatments so that the twist period or handedness varies in different regions of the film. For example, in our simulations, varying P over time has an effect similar to experimentally ramping the temperature over time to crystallize banded spherulites with variably spaced bands and oppositely twisting lamella, as has been done in PTT films [41]. Although it has not yet been achieved experimentally, spatially patterning a film with regions that favor different twisting rates by spatially varying the thickness, surface energy, composition, or temperature of the film could also potentially provide a pathway for engineering more complex twisting or curving crystallization patterns.

IV. CONCLUSION

In this paper we have presented a parametric study of twisted crystal growth in organic thin films using a phase-field model that energetically favors twisting about and along particular 3D axes, allowing us to reproduce morphologies such as banded spherulites and curved dendrites. Heterochiral banded spherulites were simulated by favoring twisting of the crystalline orientation about the fast-growing crystalline direction and along the local growth direction. In curved dendrites, we found that the turning of the dendrite branches affects both the crystallization morphology and kinetics. The total crystallized area is maximized for a finite turning rate because turning promotes side branch growth into as-yet uncrystallized regions but also ultimately leads to an isotropic growth envelope that eventually slows growth due to diffusion limitations. Interestingly, both heterochiral banded spherulites and curved dendrites require that twisting occurs along the growth direction, implying that for these morphologies the local growth conditions at the crystal-amorphous interface play an important role in how crystallization proceeds, and the structure of the crystalline phase does not by itself lead to the observed twisting patterns.

Although our model can capture a wide variety of morphologies, organic thin film crystallization is a complex process, and there are still many experimentally observed crystallization patterns that cannot be reproduced by our simple model [48, 49]. For example,

poly(propylene adipate) films crystallize with lamella winding helically about a cylinder, requiring additional parameters to fully describe the lamellar shape and orientation [50]. Films may also exhibit irregularities in surface height, such as when edge-on lamella rise above the film thickness of the melt [51], but our simulations have all been performed in two dimensions without explicitly accounting for thickness variations or surface effects. Here we have also not accounted for crystalline symmetries other than through the introduction of a k -fold-symmetric mobility anisotropy, nor does our model explicitly account for the width and thickness of lamella in banded spherulites. Nevertheless, our simulations have successfully reproduced a variety of twisting and curving crystallization patterns, and we hope that our work proves useful in the continued study of the complex crystallization behavior of organic thin films.

Appendix A: Finite volume formulas

Spatial derivatives of the quaternion field are implemented with a finite volume approach that uses Simpson’s rule for integration. Below, q refers to one of the four components of the quaternion vector \vec{q} , and t refers to the corresponding component of the twist rate \vec{t} .

For the case where $\hat{s} = \hat{x}_c = (g_{11}, g_{12})$:

$$\begin{aligned}
& \left\{ \vec{\nabla} \cdot \left[p(\phi) \left(\vec{\nabla} q - t \hat{x}_c \right) \right] \right\}_{j,k} = \\
& \frac{1}{\Delta x^2} \left[\frac{2}{3} p(\phi_{j+\frac{1}{2},k}) \left(q_{j+1,k} - q_{j,k} - t_{j+\frac{1}{2},k} \frac{g_{11,j,k} + g_{11,j+1,k}}{2} \right) \right. \\
& + \frac{2}{3} p(\phi_{j-\frac{1}{2},k}) \left(q_{j-1,k} - q_{j,k} - t_{j-\frac{1}{2},k} \frac{-g_{11,j,k} - g_{11,j-1,k}}{2} \right) \\
& + \frac{2}{3} p(\phi_{j,k+\frac{1}{2}}) \left(q_{j,k+1} - q_{j,k} - t_{j,k+\frac{1}{2}} \frac{g_{12,j,k} + g_{12,j,k+1}}{2} \right) \\
& + \frac{2}{3} p(\phi_{j,k-\frac{1}{2}}) \left(q_{j,k-1} - q_{j,k} - t_{j,k-\frac{1}{2}} \frac{-g_{12,j,k} - g_{12,j,k-1}}{2} \right) \\
& + \frac{1}{3\sqrt{2}} p(\phi_{j+\frac{1}{2},k+\frac{1}{2}}) \left(q_{j+1,k+1} - q_{j,k} - t_{j+\frac{1}{2},k+\frac{1}{2}} \frac{g_{11,j,k} + g_{12,j,k} + g_{11,j+1,k+1} + g_{12,j+1,k+1}}{2} \right) \\
& + \frac{1}{3\sqrt{2}} p(\phi_{j-\frac{1}{2},k+\frac{1}{2}}) \left(q_{j-1,k+1} - q_{j,k} - t_{j-\frac{1}{2},k+\frac{1}{2}} \frac{-g_{11,j,k} + g_{12,j,k} - g_{11,j-1,k+1} + g_{12,j-1,k+1}}{2} \right) \\
& + \frac{1}{3\sqrt{2}} p(\phi_{j+\frac{1}{2},k-\frac{1}{2}}) \left(q_{j+1,k-1} - q_{j,k} - t_{j+\frac{1}{2},k-\frac{1}{2}} \frac{g_{11,j,k} - g_{12,j,k} + g_{11,j+1,k-1} - g_{12,j+1,k-1}}{2} \right) \\
& \left. + \frac{1}{3\sqrt{2}} p(\phi_{j-\frac{1}{2},k-\frac{1}{2}}) \left(q_{j-1,k-1} - q_{j,k} - t_{j-\frac{1}{2},k-\frac{1}{2}} \frac{-g_{11,j,k} - g_{12,j,k} - g_{11,j-1,k-1} - g_{12,j-1,k-1}}{2} \right) \right]
\end{aligned}$$

For the case where $\hat{s} = \hat{n} = \frac{-\vec{\nabla}\phi}{|\vec{\nabla}\phi|} = \left(\frac{-\frac{\partial\phi}{\partial x}}{|\vec{\nabla}\phi|}, \frac{-\frac{\partial\phi}{\partial y}}{|\vec{\nabla}\phi|} \right)$:

$$\begin{aligned}
& \left\{ \vec{\nabla} \cdot \left[p(\phi) \left(\vec{\nabla} q + t \frac{\vec{\nabla} \phi}{|\vec{\nabla} \phi|} \right) \right] \right\}_{j,k} = \\
& \frac{1}{\Delta x^2} \left[\frac{2}{3} p(\phi_{j+\frac{1}{2},k}) \left(q_{j+1,k} - q_{j,k} + t_{j+\frac{1}{2},k} \frac{\phi_{j+1,k} - \phi_{j,k}}{\sqrt{(\phi_{j+1,k} - \phi_{j,k})^2 + (\phi_{j+\frac{1}{2},k+\frac{1}{2}} - \phi_{j+\frac{1}{2},k-\frac{1}{2}})^2}} \right) \right. \\
& + \frac{2}{3} p(\phi_{j-\frac{1}{2},k}) \left(q_{j-1,k} - q_{j,k} + t_{j-\frac{1}{2},k} \frac{\phi_{j-1,k} - \phi_{j,k}}{\sqrt{(\phi_{j-1,k} - \phi_{j,k})^2 + (\phi_{j-\frac{1}{2},k+\frac{1}{2}} - \phi_{j-\frac{1}{2},k-\frac{1}{2}})^2}} \right) \\
& + \frac{2}{3} p(\phi_{j,k+\frac{1}{2}}) \left(q_{j,k+1} - q_{j,k} + t_{j,k+\frac{1}{2}} \frac{\phi_{j,k+1} - \phi_{j,k}}{\sqrt{(\phi_{j,k+1} - \phi_{j,k})^2 + (\phi_{j+\frac{1}{2},k+\frac{1}{2}} - \phi_{j-\frac{1}{2},k+\frac{1}{2}})^2}} \right) \\
& + \frac{2}{3} p(\phi_{j,k-\frac{1}{2}}) \left(q_{j,k-1} - q_{j,k} + t_{j,k-\frac{1}{2}} \frac{\phi_{j,k-1} - \phi_{j,k}}{\sqrt{(\phi_{j,k-1} - \phi_{j,k})^2 + (\phi_{j+\frac{1}{2},k-\frac{1}{2}} - \phi_{j-\frac{1}{2},k-\frac{1}{2}})^2}} \right) \\
& + \frac{1}{3\sqrt{2}} p(\phi_{j+\frac{1}{2},k+\frac{1}{2}}) \left(q_{j+1,k+1} - q_{j,k} + t_{j+\frac{1}{2},k+\frac{1}{2}} \frac{\phi_{j+1,k+1} - \phi_{j,k}}{\sqrt{\frac{(\phi_{j+1,k+1} - \phi_{j,k})^2 + (\phi_{j+1,k} - \phi_{j,k+1})^2}{2}}} \right) \\
& + \frac{1}{3\sqrt{2}} p(\phi_{j+\frac{1}{2},k-\frac{1}{2}}) \left(q_{j+1,k-1} - q_{j,k} + t_{j+\frac{1}{2},k-\frac{1}{2}} \frac{\phi_{j+1,k-1} - \phi_{j,k}}{\sqrt{\frac{(\phi_{j+1,k-1} - \phi_{j,k})^2 + (\phi_{j+1,k} - \phi_{j,k-1})^2}{2}}} \right) \\
& + \frac{1}{3\sqrt{2}} p(\phi_{j-\frac{1}{2},k+\frac{1}{2}}) \left(q_{j-1,k+1} - q_{j,k} + t_{j-\frac{1}{2},k+\frac{1}{2}} \frac{\phi_{j-1,k+1} - \phi_{j,k}}{\sqrt{\frac{(\phi_{j-1,k+1} - \phi_{j,k})^2 + (\phi_{j-1,k} - \phi_{j,k+1})^2}{2}}} \right) \\
& \left. + \frac{1}{3\sqrt{2}} p(\phi_{j-\frac{1}{2},k-\frac{1}{2}}) \left(q_{j-1,k-1} - q_{j,k} + t_{j-\frac{1}{2},k-\frac{1}{2}} \frac{\phi_{j-1,k-1} - \phi_{j,k}}{\sqrt{\frac{(\phi_{j-1,k-1} - \phi_{j,k})^2 + (\phi_{j-1,k} - \phi_{j,k-1})^2}{2}}} \right) \right]
\end{aligned}$$

Values at half grid points are calculated by averaging the closest on-grid neighboring points.

ACKNOWLEDGMENTS

This work was partly supported by an NSF-DMR Grant No. 0819860 (Princeton Center for Complex Materials, a Materials Research Center) and by the National Science Foundation Graduate Research Fellowship under Grant No. DGE 1148900. Useful discussions with A. Hiszpanski and Y.-L. Loo are gratefully acknowledged. The authors would also like to thank Sarah Morgeson for helpful discussions and her contributions during the initial stages of this

work.

-
- [1] Y.-X. Liu and E.-Q. Chen, *Coordination Chemistry Reviews* **254**, 1011 (2010).
 - [2] A. M. Hiszpanski and Y.-L. Loo, *Energy Environ. Sci.* **7**, 592 (2014).
 - [3] A. G. Shtukenberg, Y. O. Punin, A. Gujral, and B. Kahr, *Angewandte Chemie International Edition* **53**, 672 (2014).
 - [4] B. Lotz and S. Z. D. Cheng, *Polymer* **46**, 577 (2005).
 - [5] E. Gunn, R. Sours, J. B. Benedict, W. Kaminsky, and B. Kahr, *J. Am. Chem. Soc.* **128**, 14234 (2006).
 - [6] X. Cui, A. G. Shtukenberg, J. Freudenthal, S. Nichols, and B. Kahr, *J. Am. Chem. Soc.* **136**, 5481 (2014).
 - [7] X. Wang and R. E. Prudhomme, *Macromolecules* **47**, 668 (2014).
 - [8] D. Maillard and R. E. Prudhomme, *Macromolecules* **43**, 4006 (2010).
 - [9] H. D. Keith and F. J. Padden Jr., *Polymer* **25**, 28 (1984).
 - [10] H. D. Keith and F. J. Padden Jr., *Macromolecules* **29**, 7776 (1996).
 - [11] J. M. Schultz, *Polymer* **44**, 433 (2003).
 - [12] J. M. Schultz, *Macromolecules* **45**, 6299 (2012).
 - [13] Y. O. Punin, *Journal of Structural Chemistry* **35**, 616 (1994).
 - [14] H.-M. Ye, J.-S. Wang, S. Tang, J. Xu, X.-Q. Feng, B.-H. Guo, X.-M. Xie, J.-J. Zhou, L. Li, Q. Wu, and G.-Q. Chen, *Macromolecules* **43**, 5762 (2010).
 - [15] Y. Hatwalne and M. Muthukumar, *Phys. Rev. Lett.* **105**, 107801 (2010).
 - [16] B. Sadlik, *The Role of Viscosity in Banded-Spherulitic Growth*, Master's thesis, Department of Physics, Simon Fraser University (2004).
 - [17] L. Gránásy, L. Rátkai, A. Szállás, B. Korbuly, G. I. Tóth, L. Környei, and T. Pusztai, *Metallurgical and Materials Transactions A* **45**, 1694 (2014).
 - [18] T. Kyu, H.-W. Chiu, A. J. Guenthner, Y. Okabe, H. Saito, and T. Inoue, *Phys. Rev. Lett.* **83**, 2749 (1999).
 - [19] X.-D. Wang, J. Ouyang, J. Su, and W. Zhou, *Chinese Physics B* **23** (2014).
 - [20] R. Mehta, W. Keawwattana, A. L. Guenthner, and T. Kyu, *Phys. Rev. E* **69**, 061802 (2004).
 - [21] R. Kobayashi, *Physica D* **63**, 410 (1993).

- [22] T. Pusztai, G. Bortel, and L. Gránásy, Europhys. Lett. **71**, 131 (2005).
- [23] T. Pusztai, G. Tegze, G. I. Tóth, L. Környei, G. Bansel, Z. Fan, and L. Gránásy, Journal of Physics: Condensed Matter **20**, 404205 (2008).
- [24] J.-L. Fattebert, M. E. Wickett, and P. E. A. Turchi, Acta Materialia **62**, 89 (2014).
- [25] M. R. Dorr, J.-L. Fattebert, M. E. Wickett, J. F. Belak, and P. E. A. Turchi, Journal of Computational Physics **229**, 626 (2010).
- [26] R. Oda, I. Huc, M. Schmutz, S. J. Candau, and F. C. MacKintosh, Nature **399**, 566 (1999).
- [27] M. Plapp, Philosophical Magazine **91**, 25 (2011).
- [28] A. M. Hiszpanski, S. S. Lee, H. Wang, A. R. Woll, C. Nuckolls, and Y.-L. Loo, ACS Nano **7**, 294 (2013).
- [29] A. Fang and M. Haataja, Phys. Rev. E **89**, 022407 (2014).
- [30] A. Fang, A. K. Hailey, A. Grosskopf, J. E. Anthony, Y.-L. Loo, and M. Haataja, APL Materials **3**, 036107 (2015).
- [31] K. Aguenau, *Modeling of Solidification*, Ph.D. thesis, Department of Physics, McGill University (1997).
- [32] In the case of solidification of a pure material, $u = (T - T_M)/(T_M - T_\infty)$, where T_M denotes the melting temperature, T_∞ denotes the initial temperature, and $\Delta = (T_M - T_\infty)/(L/c_V)$, with L and c_V denoting the latent heat and heat capacity at constant volume, respectively. Now, setting $u = -1$ everywhere and employing $\Delta < 1$ implies that excess heat accumulates ahead of the crystal-melt interface, and a fraction Δ of the system crystallizes and coexists with a melt at dimensionless temperature $u = 0$ at the end of the solidification process. On the other hand, setting $\Delta > 1$ implies that the whole system crystallizes and reaches a dimensionless temperature $u = -1 + 1/\Delta$ asymptotically.
- [33] S. S. Lee, S. B. Tang, D.-M. Smilgies, A. R. Woll, M. A. Loth, J. M. Mativetsky, J. E. Anthony, and Y.-L. Loo, Adv. Mater. **24**, 2692 (2012).
- [34] F. J. Padden Jr. and H. D. Keith, Journal of Applied Physics **30**, 1479 (1959).
- [35] S. M. LaValle, “Planning algorithms,” (Cambridge University Press, 2006) pp. 198 – 199.
- [36] L. Vicci, TR01-014, Department of Computer Science, University of North Carolina, Chapel Hill (2001).
- [37] J. A. Warren, R. Kobayashi, A. E. Lobkovsky, and W. C. Carter, Acta Materialia **51**, 6035 (2003).

- [38] A. Shtukenberg, E. Gunn, M. Gazzano, J. Freudenthal, E. Camp, R. Sours, E. Rosseeva, and B. Kahr, *ChemPhysChem* **12**, 1558 (2011).
- [39] A. G. Shtukenberg, Y. O. Punin, E. Gunn, and B. Kahr, *Chemical Reviews* **112**, 1805 (2011).
- [40] X. Cui, A. L. Rohl, A. Shtukenberg, and B. Kahr, *J. Am. Chem. Soc.* **135**, 3395 (2013).
- [41] M. Rosenthal, M. Burghammer, G. Bar, E. T. Samulski, and D. A. Ivanov, *Macromolecules* **47**, 8295 (2014).
- [42] L. Gránásy, T. Pusztai, G. Tegze, J. A. Warren, and J. F. Douglas, *Phys. Rev. E* **72**, 011605 (2005).
- [43] F. Zhang, J. Liu, H. Huang, B. Du, and T. He, *Eur. Phys. J. E* **8**, 289 (2002).
- [44] L. Gránásy, T. Pusztai, T. Börzsönyi, J. A. Warren, and J. F. Douglas, *Nat. Mater.* **3**, 645 (2004).
- [45] L. Gránásy, T. Pusztai, J. A. Warren, J. F. Douglas, T. Börzsönyi, and V. Ferreiro, *Nat. Mater.* **2**, 92 (2003).
- [46] A. G. Shtukenberg, X. Cui, J. Freudenthal, E. Gunn, E. Camp, and B. Kahr, *J. Am. Chem. Soc.* **134**, 6354 (2012).
- [47] A. Mamun, V. H. Mareau, J. Chen, and R. E. Prud’homme, *Polymer* **55**, 2179 (2014).
- [48] K. Jeon and R. Krishnamoorti, *Macromolecules* **41**, 7131 (2008).
- [49] E. Gunn, L. Wong, C. W. Branham, B. Marquardt, and B. Kahr, *CrystEngComm* **13**, 1123 (2011).
- [50] M. Rosenthal, J. J. Hernandez, Y. I. Odarchenko, M. Soccio, N. Lotti, E. Di Cola, M. Burghammer, and D. A. Ivanov, *Macromolecular Rapid Communications* **34**, 1815 (2013).
- [51] D. Maillard and R. E. Prud’homme, *Macromolecules* **41**, 1705 (2008).